Advances in Water Resources 171 (2023) 104352

Contents lists available at ScienceDirect

Advances in Water Resources

journal homepage: www.elsevier.com/locate/advwatres

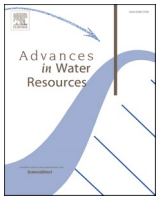

The impact of bimodal pore size distribution and wettability on relative permeability and capillary pressure in a microporous limestone with uncertainty quantification

Guanglei Zhang *, Sajjad Foroughi, Ali Q. Raeini, Martin J. Blunt, Branko Bijeljic

Department of Earth Science and Engineering, Imperial College London, London SW7 2BP, UK

ARTICLE INFO

Keywords:
Multiphase flow
Bimodal porosity
Wettability
Capillary end effect

ABSTRACT

Pore-scale X-ray imaging combined with a steady-state flow experiment was used to study the displacement processes during waterflooding in an altered-wettability carbonate, Ketton limestone, with more than two orders of magnitude difference in pore size between macropores and microporosity. We simultaneously characterized macroscopic and local multiphase flow parameters, including relative permeability, capillary pressure, wettability, and fluid occupancy in pores and throats. An accurate method was applied for porosity and fluid saturation measurements using greyscale based differential imaging without image segmentation. The relative permeability values were corrected by considering the measured saturation profile along the sample length to account for the so-called capillary end effect. The behaviour of relative permeability and capillary pressure was compared to other measurements in the literature to demonstrate the combined effects of wettability and pore structure. Typical oil-wet behaviour in resolvable macropores was measured from contact angle, fluid occupancy and curvature. The capillary pressure was negative while the oil relative permeability dropped quickly as oil was drained to low saturation and flowed through connected oil layers. Brine initially largely flowed through water-wet microporosity, and then filled the centre of large oil-wet pore bodies. Thus, the brine relative permeability remained exceptionally low until brine formed a connected flow path in the macropores leading to a substantial increase in relative permeability. Overall, this work demonstrates that not only wettability but also pore size distribution and microporosity have significant impact on displacement processes.

1. Introduction

Multiphase flow in porous media is encountered in many natural and industrial processes (Blunt, 2017), such as in soil contamination and remediation (Parker, 1989; Bear and Cheng, 2010), CO_2 (Benson and Cole, 2008; Boot-Handford et al., 2014) and H_2 (Zivar et al., 2021) storage, hydrocarbon recovery (Gerritsen and Durlofsky, 2005), as well as gas and water transport in fuel cells (Niu et al., 2007). In these processes, understanding the pore-scale fluid displacement, which depends on pore geometry and wettability, is of vital importance.

In recent years, pore-scale X-ray imaging has been combined with core flooding experiments to study multiphase flow in porous media (Blunt et al., 2013; Wildenschild and Sheppard, 2013). This technique characterizes not only macroscopic multiphase flow parameters (relative permeability, capillary pressure) but also provides insight into the pore-by-pore fluid distribution and wettability. Pioneering X-ray imaging-based work includes calculation of capillary pressure from interfacial curvature (Armstrong et al., 2012; Andrew et al., 2014b; Garing et al., 2017), measurement of relative permeability including the effect of intermittency (Gao et al., 2017; Zou et al., 2018a; Zou et al., 2018b; Gao et al., 2019; Spurin et al., 2021), characterization of wettability by contact angle measurements (Andrew et al., 2014a; Klise et al., 2016; Alhammadi et al., 2017; AlRatrout et al., 2017; Scanziani et al., 2017; Blunt et al., 2019; Sun et al., 2020), and studies of dynamic displacement phenomena (Berg et al., 2013; Andrew et al., 2015; Pak et al., 2015; Rücker et al., 2019; Scanziani et al., 2020).

The key determinants controlling local and macroscopic behaviour are pore geometry (including topology) and wettability. In particular it is difficult to predict the multiphase flow behaviour in complex rocks with broad pore size distributions (Arns et al., 2005; Bultreys et al., 2015; Pak et al., 2016). Previous experimental studies with pore-scale X-ray imaging have mostly been reported on multiphase flow in

* Corresponding author.
E-mail address: guanglei.zhang@imperial.ac.uk (G. Zhang).

https://doi.org/10.1016/j.advwatres.2022.104352
Received 6 July 2022; Received in revised form 6 September 2022; Accepted 14 November 2022
Available online 17 November 2022

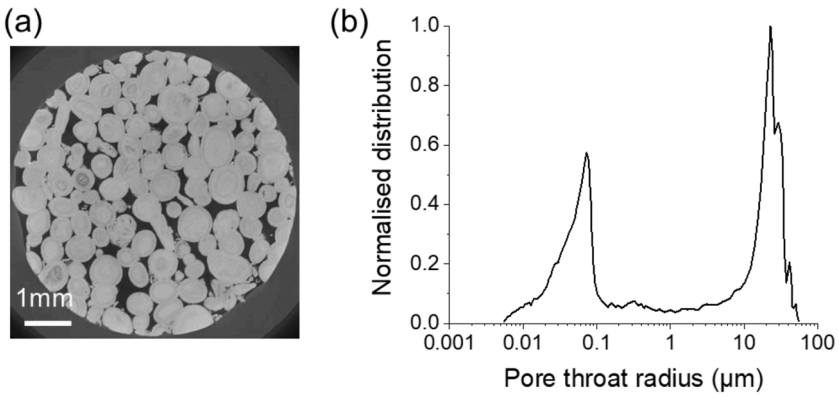

Fig. 1. (a) A two-dimensional cross-section of a three-dimensional greyscale image, and (b) the bimodal pore size distribution of Ketton limestone measured by the mercury injection capillary pressure (MICP) method: there is almost three orders of magnitude variation between the peak of the throat radius distribution in microporosity below 0.1 μm, and the peak in the macropores, above 10 μm.

homogeneous sandstone rocks with unimodal pore size distributions (Gao et al., 2017; Lin et al., 2018; Zou et al., 2018a; Zou et al., 2018b; Lin et al., 2019; Gao et al., 2021); only a few experimental studies exist on more complex rock geometries such as the ones commonly encountered in carbonates (Gao et al., 2019; Alhammadi et al., 2020; Lin et al., 2021). Here the impact of geometry can be profoundly different, notably by the interplay between flow through microporosity (with pore radii of less than approximately 1 micron, below the resolution of our images) and macropores (pores larger than a few microns that can be resolved in the images). Furthermore, relative permeability in all these studies has not been thoroughly assessed in terms of measurement uncertainty, which is needed for experimental data evaluation, and image-based calibration and validation of pore-scale modelling tools (Raeini et al., 2022).

The main aim of this study is to provide new multiphase flow measurements with complex geometry and wettability and to discuss the unique features related to contact angle, pore occupancy, curvature, capillary pressure and relative permeability through comparison with other datasets in the literature. We will examine the impact of a bimodal pore size distribution on multiphase flow and displacement in a microporous limestone whose wettability has been altered from a water-wet state. By bimodal pore size distribution, we mean a complete separation of length scales in microporosity and macropores, as shown in Fig. 1, which illustrates at least 2 orders of magnitude difference in pore sizes in Ketton limestone. Moreover, we will conduct a rigorous analysis of saturation and relative permeability using new methods that reduce and quantify measurement uncertainty while accounting for inhomogeneities in the saturation profiles. We will use a new greyscale-based differential imaging method for porosity and saturation calculations without segmentation and demonstrate its accuracy in terms of image resolution.

2. Material and methods

2.1. Rock sample and fluid properties

A cylindrical Ketton limestone sample of 6.1 mm in diameter with a length of 54.6 mm was used in this study, as shown in Fig. 1. The sample is mainly composed of calcite mineral (>99%) and has a helium porosity of 0.239 ± 0.008. The absolute permeability of the sample was measured based on Darcy's law at three flow rates under single-phase (brine) conditions to be 2.45 ± 0.03 Darcy.

The oil phase was decane that has a density of 730 kg/m^3 (n-Decane, Acros Organics) and a viscosity of 0.838 mPa•s (provided by PubChem, open chemistry database). The brine phase was deionised water doped with 25 wt% Potassium Iodide (KI) with a viscosity of 0.82 ± 0.01 mPa•s. The 25 wt% KI was used as a high contrast dopant to distinguish the brine phase with the other two phases: oil and grain. Details concerning the contrast scans between rock and fluids can be found in Appendix A. The interfacial tension (IFT) between brine and decane was measured to be 47.05 ± 1.56 mN/m at ambient conditions using a Rame-Hart apparatus (590 F4 series) based on the pendant drop method (Andreas et al., 1938; Stauffer, 1965).

2.2. Experimental methods

This study includes three main parts: a) absolute permeability measurement, dry scan, and brine saturated scan of the sample; b) dynamic ageing of the sample through contact with crude oil at high temperature and pressure for wettability alteration; and c) a steady-state two phase flow experiment at low capillary number of 4.1×10^{-7} with a total flow rate of 0.04 ml/min. The capillary number, Ca, defined as $\mu q/\sigma$, where q is the total Darcy velocity of the injected fluids, σ is the interfacial tension between oil and brine, and μ is the average viscosity of both fluids. A Hassler type X-ray transparent flow cell made of carbon fibre epoxy was used for the steady state two-phase flow experiments (Fig. 2). Brine and decane were injected simultaneously into the sample with controlled flow rates while measuring the pressure differential across the sample by a high accuracy transducer (Keller PD-33X). The pore pressure was controlled by a back pressure regulator (Equilibar zero flow series which could handle the range of flow rates applied) and the effluent of brine and decane was collected at the outlet of the regulator.

The step-by-step workflow of this experiment was as follows.

1 The sample was put into the Viton sleeve and then assembled in the core holder. Polyether ether ketone (PEEK) lines were connected between the core holder within the micro-CT scanner and the pumps outside.
2 Deionized water as the confining fluid was injected and filled the space between the Viton sleeve and the carbon fibre sleeve. A confining pressure of 2 MPa was applied step by step to squeeze the Viton sleeve onto the sample to avoid bypass flow between the sample and the sleeve.
3 The dry sample was imaged by four coarser resolution scans for covering the full sample length, two high resolution scans in the middle and one high resolution scan near the outlet of the sample. The scanning locations are shown in Fig. 2. The voxel sizes of coarser resolution and high-resolution images were 8.91 μm and 3.58 μm, respectively. The overlap between one scan to the neighbour for both coarser resolution images and high resolution images was approximately 30% in order to stich neighbouring scans together.
4 More than 200 pore volumes 25 wt% KI brine was injected to displace air in the pore space and ensure the sample was fully

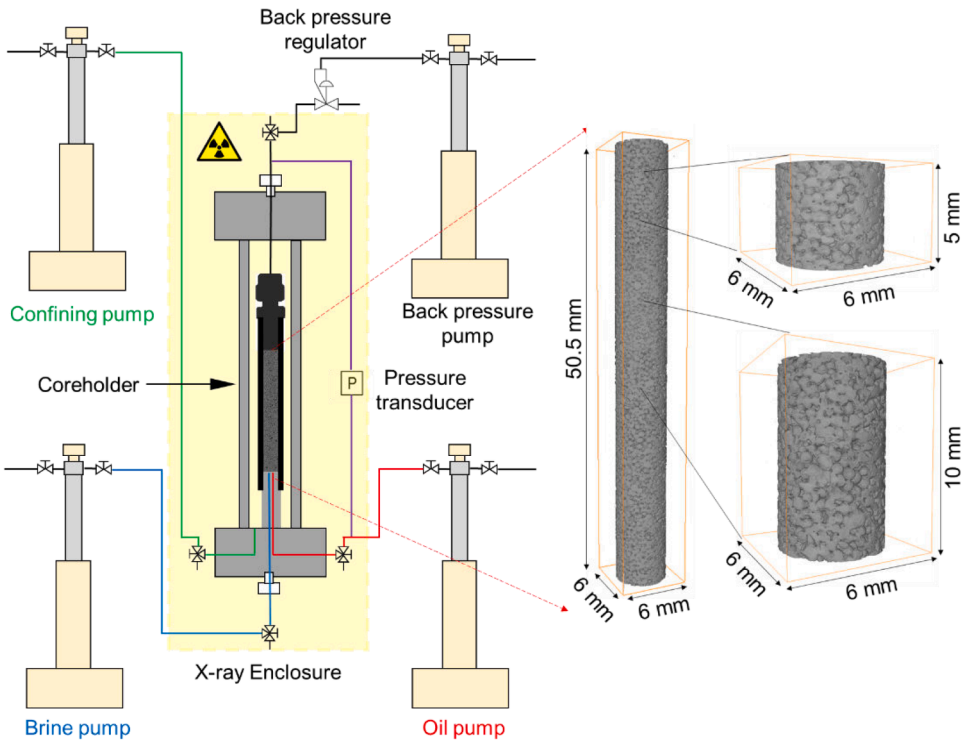

Fig. 2. Schematic diagram of the two-phase flow system coupled with X-ray imaging. Oil and brine can be injected simultaneously into the sample from the bottom end with the designed dual injection head. Two high resolution tomographic scans with voxel size of 3.58 μm were taken in the middle section, and one was taken near the downstream (upper) end. Another four coarser resolution tomographic scans with voxel size of 8.91 μm were taken for the full length of the sample. Note that approximately 2 mm was cropped at the top and bottom of the sample with voxel size of 8.91 μm to avoid image artefacts.

saturated by brine. After that, the pore pressure was set at 1 MPa by the back pressure regulator and the confining pressure was increased to 3 MPa.

5 The pressure differential for single-phase brine injection was monitored over three flow rates to measure the absolute permeability: 2.45 ± 0.03 Darcy. A reference scan of the sample fully saturated with brine was then acquired.

6 The core holder was moved into an oven with a temperature of 80 ± 1 ℃. A pore pressure of 5 MPa and confining pressure of 7 MPa were set. The Ketton sample was maintained at these conditions for 3 days to allow ion equilibration between the solid and brine.

7 Crude oil was injected into the sample by increasing flow rate from 0.02 mL/min to 2 mL/min stepwise to reach the irreducible water saturation. This is a primary drainage process. After that, crude oil was injected at a flow rate of 0.001 mL/min for a period of 3 weeks. This process is called ageing during which the wettability of the sample changes to mimic conditions in the deep subsurface. The composition and properties of the crude oil can be found elsewhere (Selem et al., 2021). During ageing, the flow direction was reversed half way through to establish a uniform initial brine saturation and homogeneous wettability alteration. At the end of ageing, decalin was first injected into the sample to displace the crude oil and then decane was injected to displace decalin. This was done to avoid asphaltene precipitation.

8 After ageing, the pore pressure was decreased to 1 MPa and the confining pressure was decreased to 3 MPa. The core holder was then isolated by closing the three-way valve. The core holder was disconnected from the tubing and moved back to the micro-CT scanner. The pumps were then connected again to the core holder and air was flushed out of the lines through the three-way valves to avoid any air entering the system.

9 Brine and decane were injected simultaneously into the sample at different fractional flows, the ratio of the volumetric brine flow rate to the total flow rate of oil and brine ($f_w = 0$, 0.05, 0.15, 0.3, 0.5, 0.7, 0.95, 1) with a constant total flow rate of 0.04 mL/min. At the last fractional flow point ($f_w = 1$) the brine flow rate was increased 100 times, from 0.04 mL/min to 4 mL/min (this is called a bump flood) for over 100 pore volumes to reach the residual oil saturation. Then brine injection continued at 0.04 mL/min to measure the pressure differential when the fractional flow was 1.

10 For each fractional flow, injection continued for at least 20 h to reach a steady-state condition, which was indicated by a stable and constant pressure drop for at least 6 h monitored by the differential pressure transducer. Once steady state was reached, X-ray images were taken at the same position as described in Step 3 without stopping fluid injection to investigate the fluid saturation and configuration in the pore space. For the last fractional flow point ($f_w = 1$), X-ray images were taken twice: before and after the higher rate (bump) flood.

11 The sample was taken out the core holder and all eight fractional flows were repeated but without the rock sample (or imaging) to measure the pressure differential in the flow lines. A rigorous tubing (line) pressure validation and uncertainty analysis were conducted, see Appendices B and C.

2.3. Imaging methods and processing

The images were taken using a Zeiss XRM-510 X-ray CT scanner with a flat panel detector. The X-ray energy was 80 KeV and the power was 7 W. The exposure time was set to 1.60 s and the number of projections for each scan was 3201 to enhance image quality. All tomograms were reconstructed into three-dimensional images using the Zeiss Reconstructor Software. At each fractional flow, the four coarser images with 8.91 μm voxel size were normalized to the brine-saturated images slice by slice, as a reference, and stitched to the whole sample, as shown in Fig. 2. The stitched image size was $6 \times 6 \times 50.5$ mm^3. Similarly, the overlapping images of two high resolution images in the middle of the sample were also normalized to the brine-saturated images and stitched together, as shown in Fig. 2. The stitched image size was $6 \times 6 \times 10$ mm^3. All images were registered to the brine-saturated image with the same position.

Instead of segmentation, which has user bias, we conducted greyscale-based calculations of porosity and saturation without

Table 1
Measurements, methods and the corresponding image size and voxel size.

Measurement	Method	Image size / mm^3	Voxel size / μm
Porosity / saturation	Greyscale-based differential imaging	6 × 6 × 50.5	8.91
Contact angle	Segmentation	3.58 × 3.58 × 3.58	3.58
Fluid occupancy	Segmentation	3.58 × 3.58 × 3.58	3.58
Mean / Gaussian curvature	Segmentation	2 × 2 × 2	3.58

segmentation, as proposed by Withjack (1988) and applied to a wide range of rock types (Krevor et al., 2012; Akbarabadi and Piri, 2013; Vega et al., 2014; Pini and Madonna, 2016). We combine greyscale-based calculations with differential imaging. The solid and brine phases cancel out during differential imaging – subtracting the brine saturated image from the dry/partially-saturated images. In this case, simpler equations to determine porosity and saturation are used with lower uncertainty (Raeini et al., 2022), see Appendix D. As for interfacial properties, image segmentation which combines differential imaging with interactive thresholding segmentation was then performed to obtain quantitative information, such as contact angle, fluid occupancy, curvature and capillary pressure. The segmentation procedure is explained in more detail in Appendix E. The measurements used for this paper and the corresponding methods, image size and voxel size are described in Table 1.

3. Results and discussion

We start with the characterization of pore structure in Section 3.1 followed by measurement of porosity and fluid saturation by greyscale-based differential imaging without segmentation in Section 3.2. Then we quantify the in situ wettability through the geometric contact angle in Section 3.3. This is followed by the analysis of the fluid occupancy in pores and throats in Section 3.4. In Section 3.5, we present the interfacial curvature analysis, including mean curvature and Gaussian curvature, and the calculation of capillary pressure based on mean curvature. Finally, the relative permeability and implications for recovery are presented in Section 3.6 with a discussion of other results in the literature to show how wettability and pore structure control multiphase flow properties. This analysis includes a method to account for an arbitrary inhomogeneous saturation profile, allowing for the capillary end effect and other heterogeneities present in the system.

3.1. Characterization of pore structure

We extracted network models from the stitched high-resolution images with voxel size of 3.58 μm in the middle of the sample (6 × 6 × 10 mm^3). The maximal ball method was used to divide the segmented macropores into wide regions (pores) separated by restrictions (throats) (Dong and Blunt, 2009; Raeini et al., 2017). The pore and throat radii were found from the largest sphere which can fit in the centres of the pores and throats. The sub-resolution microporosity in rock grains was not considered in the analysis, as it cannot be resolved in the images.

We compared the pore and throat size distributions of Ketton carbonate with Estaillades carbonate, a benchmark microporous carbonate for relative permeability and displacement analysis (Gao et al., 2019; Lin et al., 2021) in Fig. 3. Later in the paper we will use this information to understand the differences in capillary pressure and relative permeability characteristics for these two rocks. Ketton has larger resolvable (macro) pores and throats compared to Estaillades. In addition, we also plotted the number of pores and throats which are not connected. This means they are only connected through sub-resolution microporosity. While Estaillades has a large number of isolated pores and throats with

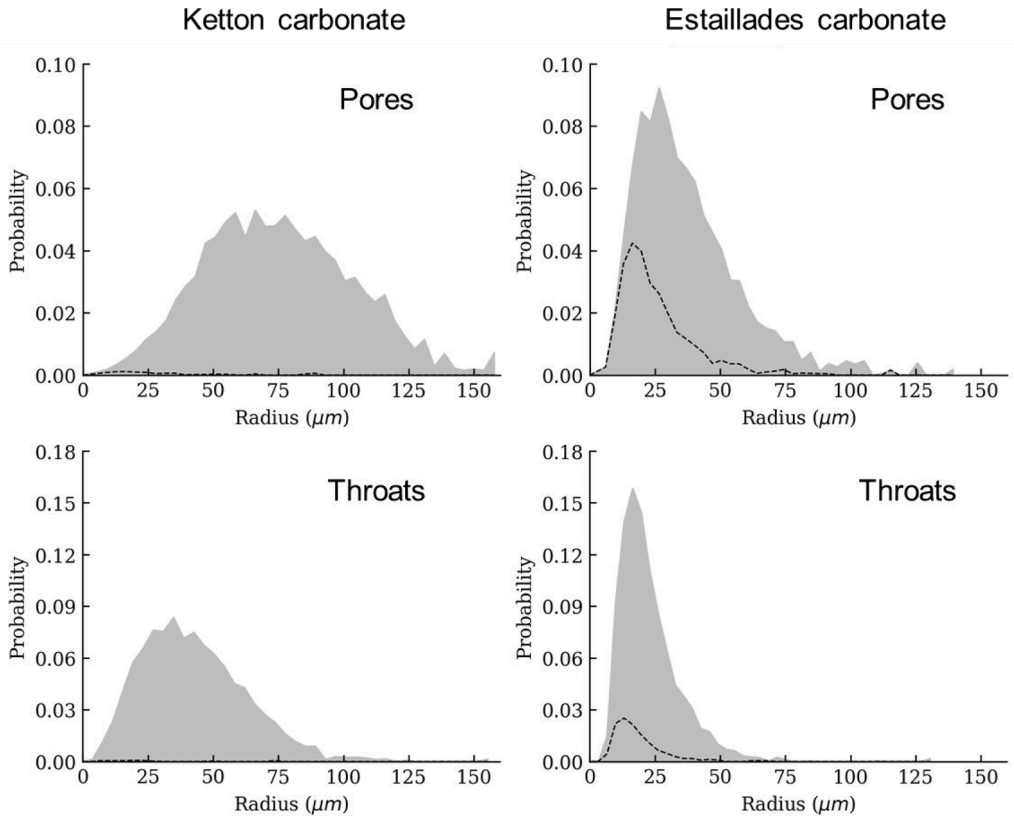

Fig. 3. The radius distributions of pores and throats comparing Ketton (pores: 13,668; throats: 24,407) and Estaillades carbonate (pores: 104,241; throats: 72,506) (Lin et al., 2021). The dashed lines indicate resolvable pores and throats which are only connected through sub-resolution microporous pores and throats.

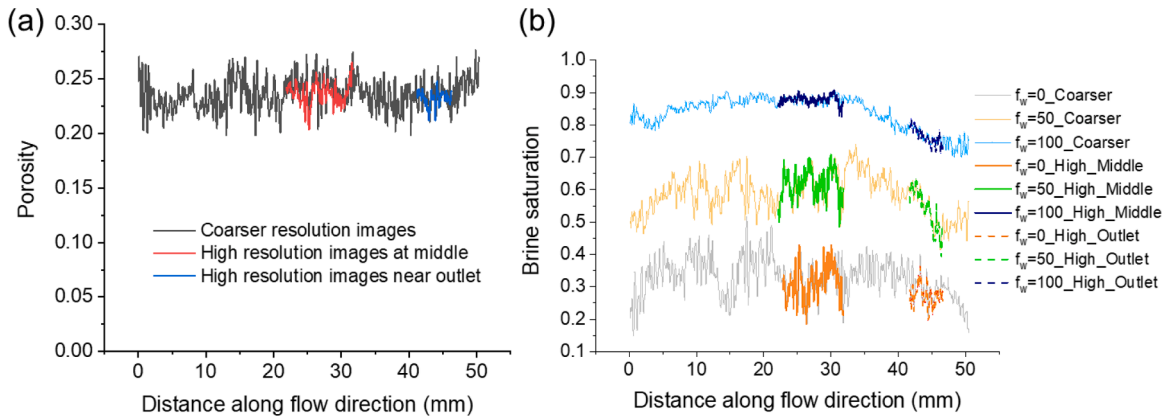

Fig. 4. (a) Comparison of the porosity profile along the sample obtained by high and coarser resolution images. (b) Comparison of the brine saturation profile along the flow direction obtained by high (bold) and coarser resolution images, where the results for three fractional flows are plotted for demonstration.

zero coordination number, for Ketton, these isolated elements are largely absent.

3.2. Porosity and saturation measurements based on greyscale images without segmentation

The porosity and saturation profiles of the coarser resolution images are compared to those of high-resolution images slice by slice at the same location in the middle of the sample and near the downstream end (Fig. 4). The results show that the coarser resolution images match well slice by slice with the high-resolution ones, which indicates the greyscale-based differential imaging method for porosity and saturation computation is accurate even at the coarser image resolution. Moreover, the average porosity obtained from the images (0.236 ± 0.008) agrees to within the uncertainty of the measurements with the helium porosity (0.239 ± 0.008), which again demonstrates the accuracy of our greyscale-based differential imaging method.

The brine saturation profiles across the whole sample for all the fractional flows are shown in Fig. 5. These profiles are based on the average greyscale values of the whole sample accounting for both brine in the macropores and unresolved microporosity. The brine saturation profile for all the fractional flows was heterogenous along the flow direction. Specifically, the brine saturation is lower near the outlet due to the so-called capillary end effect: there was retention of the preferentially wetting phase (oil) at the outlet. This heterogenous saturation profile affects the analysis of relative permeability: we will discuss how to include the effect of a heterogenous saturation profile in Section 3.6.

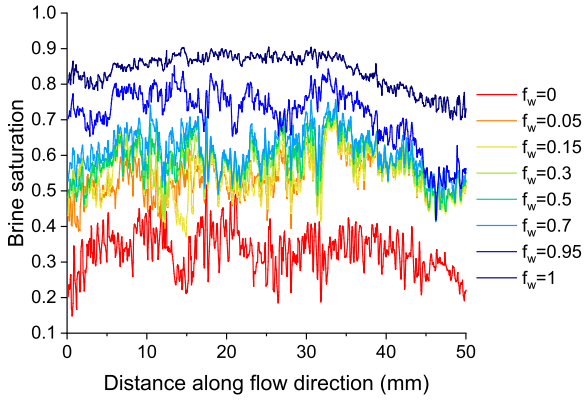

Fig. 5. The brine saturation profile based on the coarser images along the flow direction at eight fractional flows.

3.3. Wettability characterization

We measured the in situ contact angle distribution (Fig. 6) in macropores using an automated method (AlRatrout et al., 2017). The results show that there is a wide range of contact angle both above and below 90°. The peak (mode) values are between 110° and 115° for all fractional flows. Table 2 shows that the mean values of contact angles are larger than 90° and range from 95° to 115°.

The mean contact angle increases slightly as the displacement proceeds. Initially, brine will invade the more water-wet regions of the pore space, with three-phase contacts in these regions. Hence, for the lowest fractional flows we observe a significant fraction of contact angles below

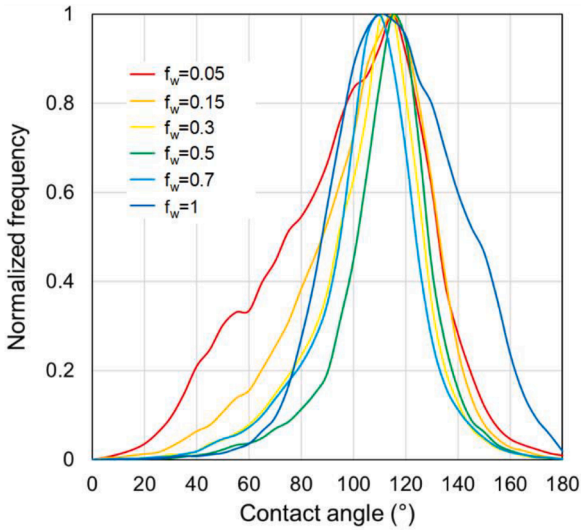

Fig. 6. The measured contact angle distributions for different fractional flows based on the segmented images.

Table 2
The geometric contact angle distributions showing the mean and standard deviation at all fractional flows.

f_w	Contact angle
0.05	95.1 ± 29.4°
0.15	102.1 ± 24.6°
0.3	103.8 ± 20.5°
0.5	109.8 ± 18.5°
0.7	103.1 ± 20.2°
1	114.8 ± 23.5°

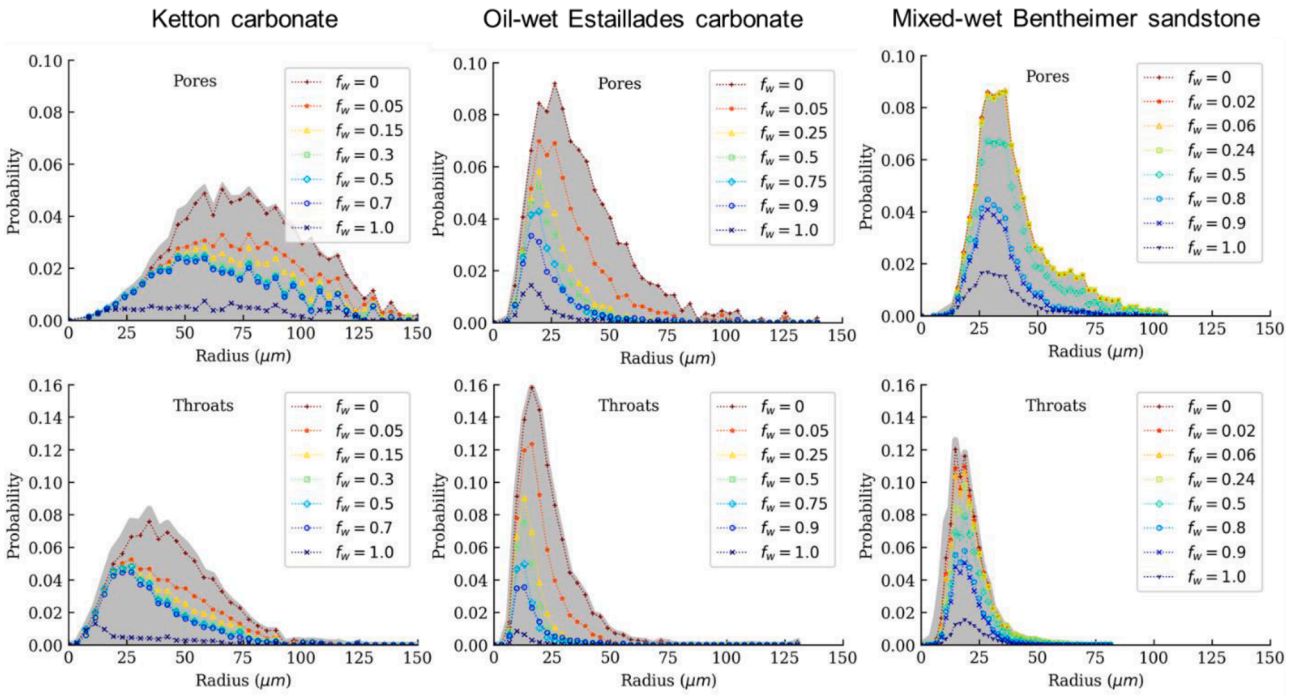

Fig. 7. Volume-weighted histogram plot showing distribution of pores and throats filled with oil during waterflooding in Ketton carbonate compared with an oil-wet Estaillades carbonate (Lin et al., 2021) and a mixed-wet Bentheimer sandstone (Lin et al., 2019). The grey areas represent the pore and throat size distributions.

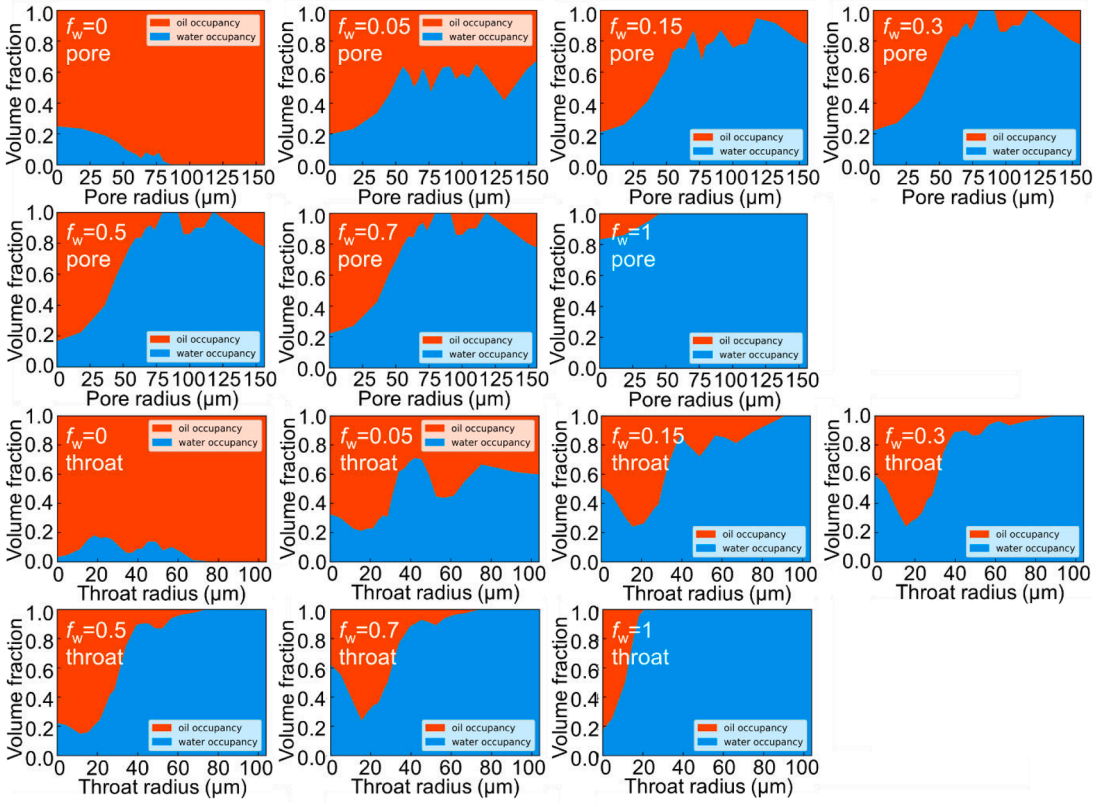

Fig. 8. The volume fraction of pore/throat radii occupied by oil (red) and brine (blue) as a function of radius.

90°. As displacement proceeds, the brine is forced into both smaller and more oil-wet regions of the pore space. At the end of waterflooding, the three-phase contact lines now reside in almost exclusively oil-wet regions of the pore space with contact angles above 90°.

3.4. Fluid occupancy in pores and throats

By using the extracted pore and throat labels described in Section 3.1, we computed the pore occupancy by calculating the fraction of oil-

filled voxels in the largest sphere at the centre of each pore and throat of the sample ($6 \times 6 \times 10$ mm^3) for all fractional flows. We define a pore to be filled if the oil fraction is larger than 50%, shown in Fig. 7. To further test how wettability impacts fluid occupancy, the pore occupancy in different sizes of pores and throats of a smaller sample volume ($3.58 \times 3.58 \times 3.58$ mm^3) are quantified in Fig. 8. The volume-weighted fraction of pores and throats whose centres were occupied by brine or oil was computed to determine the fluid occupancy. During waterflooding, brine preferentially filled the larger pores and throats first, while the smaller elements remained oil filled. This is consistent with oil-wet conditions where brine is the non-wetting phase. As shown in Fig. 7, similar behaviour – largest pores and throats to be filled with brine first – has also been seen in an oil-wet Estaillades carbonate (Lin et al., 2021). On the other hand, we observed brine filling of pores and throats of all size throughout the displacement in a mixed-wet Bentheimer sandstone (Lin et al., 2019), where smaller pores and throats in water-wet regions and larger ones in oil-wet regions were preferentially filled with brine.

3.5. Interfacial curvature and capillary pressure

Capillary pressure, defined as the pressure difference between the oil and brine phases, is calculated using the Young-Laplace equation.

$$P_c = P_o - P_w \tag{1}$$

$$P_c = 2\sigma\kappa \tag{2}$$

$$\kappa = \frac{1}{2}(\kappa_1 + \kappa_2) \tag{3}$$

where P_c is the capillary pressure, σ is the interfacial tension, κ is the mean curvature of the interface, which is the average of the two principal curvatures, κ_1 and κ_2, where we define $\kappa_1 > \kappa_2$.

The curvature was obtained by approximating the smoothed oil-brine interface locally by a quadratic form. The eigenvalues and eigenvectors of the quadratic form correspond to the principal curvature values and the directions of principal curvature, respectively. More details about interface extraction and the smoothing process can be found elsewhere (Lin et al., 2018). The smoothed oil-brine interfaces for different fractional flows are shown in Fig. 9.

Fig. 10 shows the curvature distribution of 1.3 million measured curvature values at $f_w = 0.5$. The peak of the distribution of the mean curvature is slightly negative, indicating a negative capillary pressure and, on average, oil-wet conditions. However, as with contact angle, the pore-by-pore picture is more complex. We separated the mean curvatures into three categories: 1) both principal curvatures are positive (blue), water-wet case; 2) both negative (red), oil-wet case; 3) one value is positive and the other negative (green), mixed-wet case. Approximately 70% of the interfaces have one positive curvature and one negative curvature, giving a negative Gaussian curvature (Fig. 11a), and this occurs at all fractional flows. This means that most interfaces are saddle-shaped. This potentially provides good connectivity of both oil and brine through the pore space (Khanamiri et al., 2018). It implies that the two phases can flow over a wide saturation range, indicating favourable pore-scale displacement efficiency (Lin et al., 2019; Alhammadi et al., 2020; Gao et al., 2020). This is an important observation and has been seen previously for both sandstones and carbonates with a range of contact angles both above and below 90°, as observed here (Lin et al., 2019; Alhammadi et al., 2020; Gao et al., 2020): we describe this condition as mixed-wettability (AlRatrout et al., 2018).

Fig. 11b shows the capillary pressure based on the measured mean curvature, compared with literature data from sandstones and carbonates with different wettability conditions. The capillary pressure of Ketton carbonate was negative, consistent with the mean curvature, and decreased with brine saturation as brine was principally the non-wetting phase and forced into smaller pores and throats progressively to displace oil.

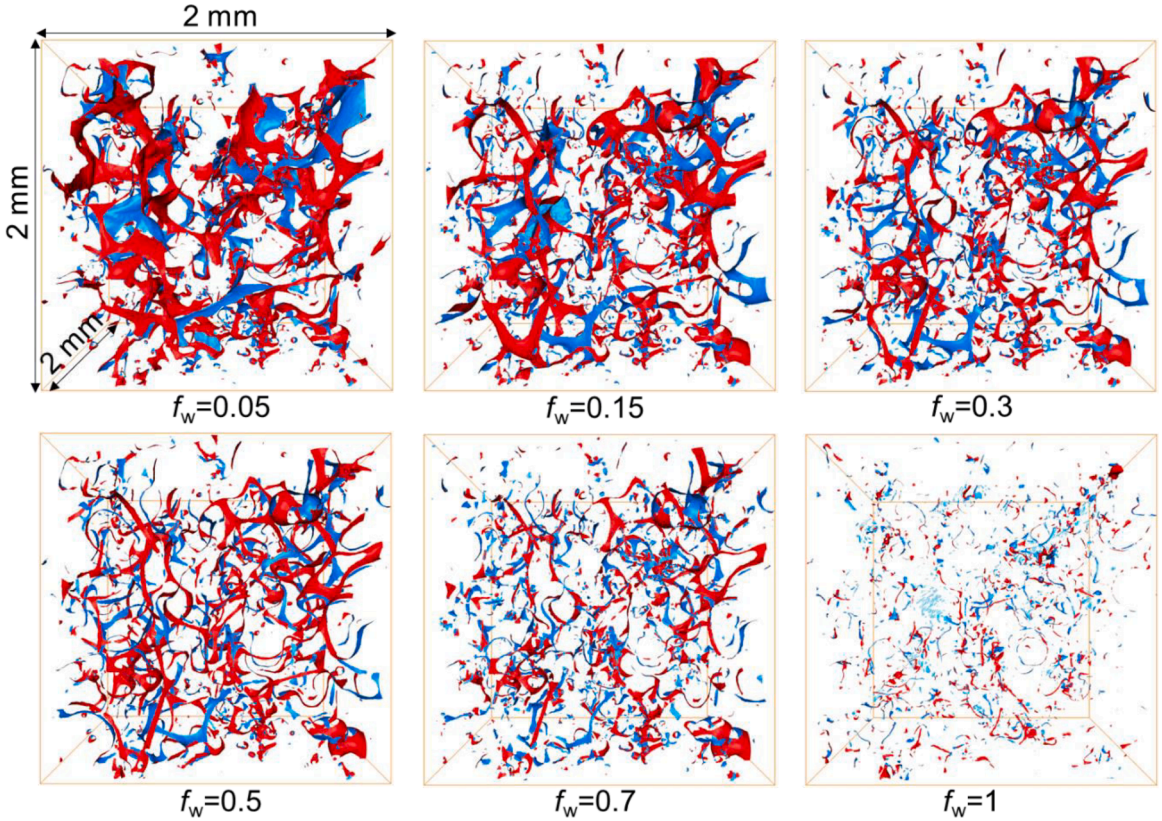

Fig. 9. The smoothed oil-brine interfaces for different fractional flows. Red indicates the side of the interface next to oil, while blue shows the interface next to water.

We observed a low mean curvature, with two approximately equal, but opposite principal curvatures in Ketton carbonate as shown in Fig. 10. Similar behaviour, with a low but slightly negative capillary pressure from menisci with principal curvatures of opposite sign has also been seen in a mixed-wet reservoir carbonate (Alhammadi et al., 2020), mixed-wet Bentheimer sandstone (Lin et al., 2019) and a mixed-wet reservoir sandstone (Gao et al., 2020). On the other hand, a more distinctly oil-wet Estaillades carbonate had a lower – more negative – capillary pressure as a consequence of a stronger wettability alteration, leading to larger contact angles (Lin et al., 2021), and differences in the pore and throat size distributions, see Fig. 3, with, on average, smaller pores than in Ketton. In the next section we will demonstrate how the combination of pore structure and wettability also affects relative permeability.

3.6. Relative permeability and implications for recovery

3.6.1. Measured relative permeability with correction for saturation heterogeneity

Darcy's law was used to calculate the steady state relative permeability.

$$k_{rw} = \frac{q_w \mu_w L}{\Delta P K} \tag{4}$$

$$k_{ro} = \frac{q_o \mu_o L}{\Delta P K} \tag{5}$$

where k_{rw} and k_{ro} are the relative permeabilities of water and oil respectively, q is the Darcy velocity, μ is the fluid viscosity, L is the sample length, ΔP is the pressure loss over length L, which was measured in the oil phase in this work, K is the absolute permeability.

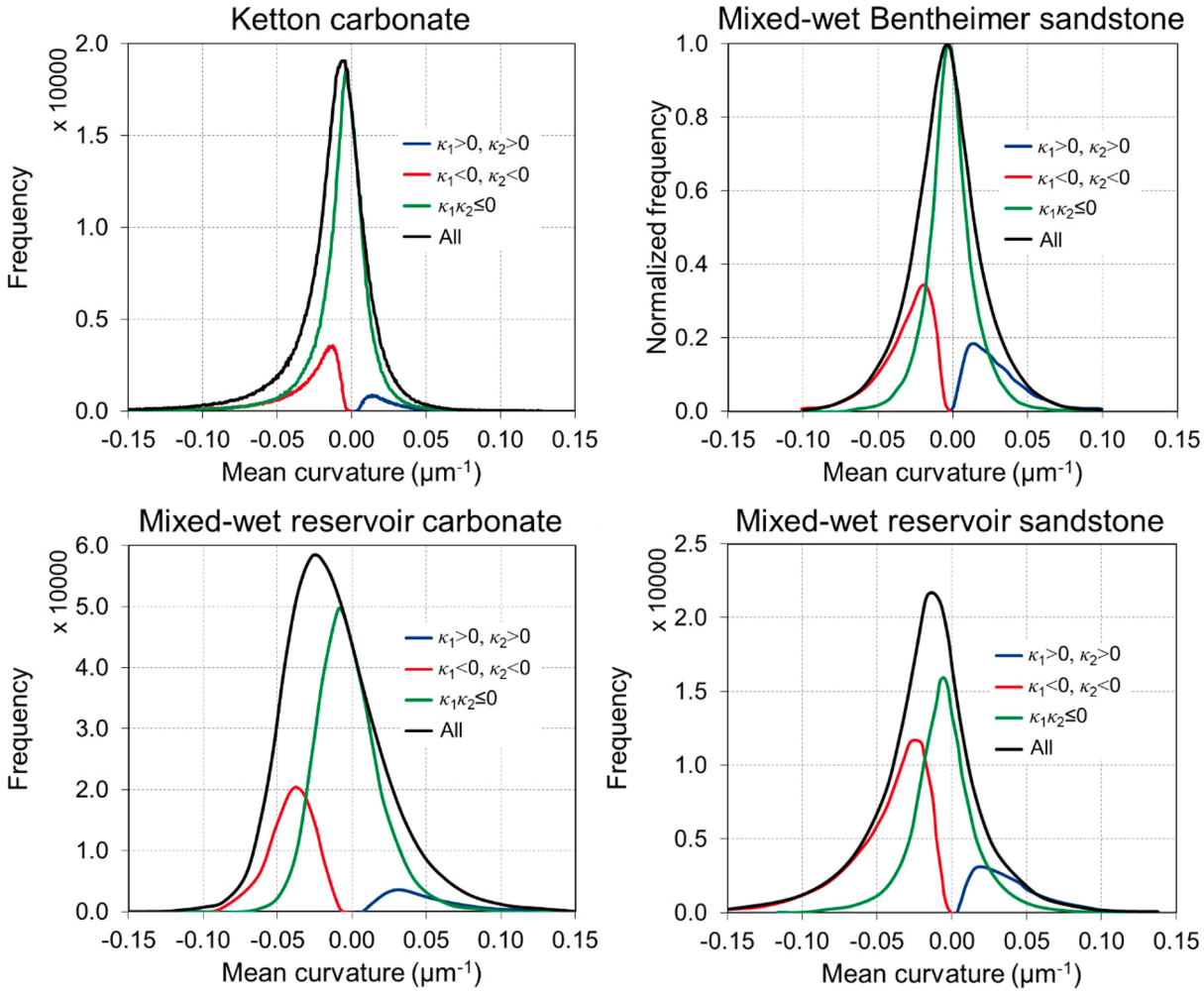

Fig. 10. Measured oil-brine mean curvature distribution at $f_w = 0.5$ in this work compared with a mixed-wet Bentheimer sandstone (Lin et al., 2019), a mixed-wet reservoir carbonate (Alhammadi et al., 2020) and a mixed-wet reservoir sandstone (Gao et al., 2020). All mean curvatures are shown in black. The distribution of values where both principal curvatures are positive (blue), $k_1 > 0$, $k_2 > 0$, both negative (red), $k_1 < 0$, $k_2 < 0$, and when one value is positive and the other negative (green), $k_1 k_2 < 0$.

The brine saturation at each fractional flow was measured on the coarser resolution greyscale images for the whole sample. As discussed in Section 3.2, the brine saturation is heterogenous along the flow direction and tends to be lower near the downstream end.

Traditionally, relative permeability in steady-state flow is calculated using Eqs. (4) and (5) assuming that the saturation profile is homogeneous with the same pressure drop in each phase (the capillary pressure is constant). These assumptions are rarely correct, as shown in Fig. 5. It is possible to account for inhomogeneities in the analysis of core floods through a quantitative assessment of local heterogeneity (Jackson et al., 2018): here we will do this using a simpler approach.

In our experiment, with a long, thin core, flow is approximately one-dimensional. A region where, locally, the saturation of one phase is low will restrict the flow of that phase, leading to locally a high pressure gradient. The average saturation over the whole core may be significantly higher, but the overall pressure drop may be dominated by these low-saturation regions. The result is that we assign a high pressure drop and hence low relative permeability to a high average saturation. There is a tendency to underestimate the relative permeability if we assume a homogeneous saturation profile.

We have developed a method that automatically accounts for an inhomogeneous saturation profile. We assume that there is a unique relative permeability as a function of saturation, defined locally in slice-averages of the image. We find this relative permeability which, when the pressure gradient is integrated along the measured saturation profile, gives the measured overall pressure drop to within the uncertainty of the measurements, see Appendices B and C. We also account for pressure differences between the phases due to differences in capillary pressure (which we have measured – see Fig. 11b) and buoyancy. The details are provided in Appendix F. The end result is a corrected relative permeability with a quantified assessment of uncertainty.

A comparison between the uncorrected (assuming a homogeneous saturation profile) and corrected relative permeability is shown in Fig. 12 and Table 3. The results indicate that the relative permeability of

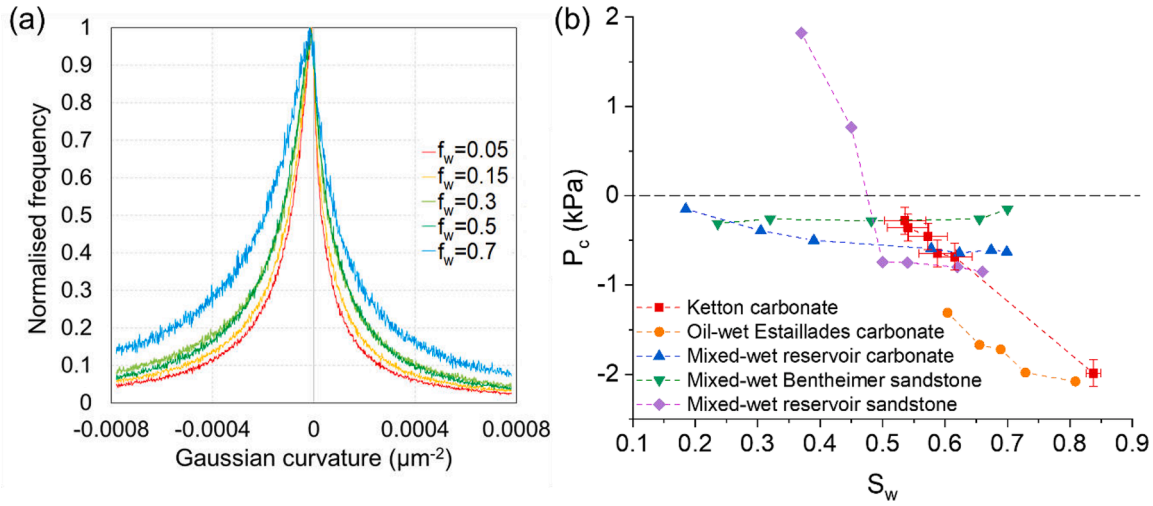

Fig. 11. (a) Gaussian curvature distribution at different fractional flows. (b) Capillary pressure for Ketton carbonate analysed in this work compared with an oil-wet Estaillades carbonate (Lin et al., 2021), a mixed-wet reservoir carbonate (Alhammadi et al., 2020), a mixed-wet Bentheimer sandstone (Lin et al., 2019) and a mixed-wet reservoir sandstone (Gao et al., 2020). The error bars indicate the measured uncertainties in the estimation of brine saturation and capillary pressure. The uncertainty of brine saturation calculation can be found in Appendix D, while the uncertainty of capillary pressure comes from the errors of mean curvature measurements from the extracted interfaces.

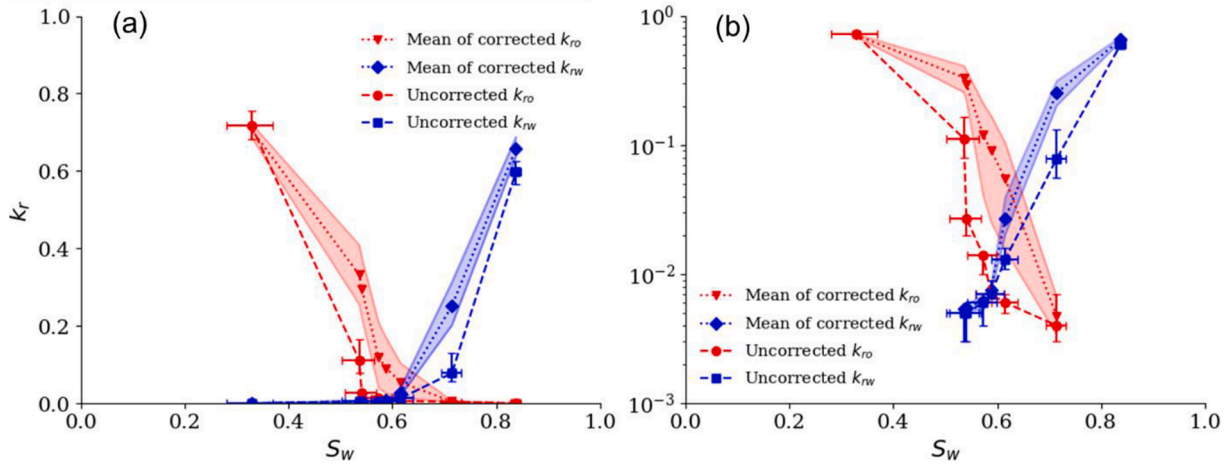

Fig. 12. The comparison between uncorrected (assuming a homogeneous saturation profile) and corrected (taking into account the measured saturation) relative permeabilities shown on a linear axis (a) and on a logarithmic axis (b). The shaded areas represent the uncertainty of the corrected oil and water relative permeability values.

Table 3
Relative permeability of the oil and brine phases with and without correction for saturation heterogeneity.

f_w	S_w	k_{ro} (uncorrected)	k_{ro} (corrected)	k_{rw} (uncorrected)	k_{rw} (corrected)
0	0.328 ± 0.048	0.718	0.708	0	0
0.05	0.536 ± 0.033	0.112	0.332	0.005	0.005
0.15	0.541 ± 0.033	0.027	0.296	0.005	0.006
0.3	0.573 ± 0.031	0.014	0.119	0.006	0.006
0.5	0.588 ± 0.030	0.007	0.091	0.007	0.008
0.7	0.615 ± 0.028	0.006	0.055	0.013	0.027
0.95	0.714 ± 0.021	0.004	0.005	0.078	0.251
1	0.838 ± 0.012	0	0	0.597	0.657

the oil and brine phases was underestimated by simply using average brine saturation in the k_r-S_w relationship, which assumes a uniform saturation profile for the whole sample.

It can be seen that the water relative permeability is low until a high saturation is reached at the last two fractional flows ($f_w = 0.95$ and $f_w = 1$). The cross-over saturation when the two relative permeabilities are equal is above 0.6, which is favourable for oil recovery; furthermore the oil drained to a low residual saturation (0.16). At the last two fractional flows, the water relative permeability increased sharply, and the final water relative permeability is high (0.66). This water relative permeability is not typical oil-wet behaviour, where invasion percolation occurs in the larger pores and the water relative permeability increases rapidly; instead we observe more percolation-like mixed-wet relative permeability characteristics (Blunt, 2017). This is the result of Ketton carbonate distinct bimodal pore size distribution (Fig. 1) and wettability, which will be described in detail in the following section.

3.6.2. Brine connectivity and its impact on water relative permeability

Fig. 13 illustrates the displacement of oil in microporosity and macropores in a small region of the sample. At the beginning of waterflooding, oil resides in macropores, as well as partially invading the microporosity, as shown in Fig. 13 from comparing the brine scan with that taken at $f_w = 0$. When waterflooding started (from $f_w = 0$ to $f_w = 0.05$), we observed brine firstly filled the microporosity (greyscale values increased), which we assume remained water-wet. We also see forced displacement of oil in an oil-wet pore at a negative capillary pressure (the water bulges out into the oil). The water flows through the microporosity to preferentially fill the larger pores throughout the sample (see Fig. 8) in a percolation-like displacement. The water relative permeability remains low, limited by flow through microporosity, until the water in the macropores connects across the pore space.

The three-dimensional volume rendering of the brine phase in macropores is shown in Fig. 14. Different colours indicate different brine clusters and the brine connectivity in the macropores of a smaller volume in the middle of the sample was quantified in Table 4. At $f_w = 0.05$, the image shows brine filled the large oil-wet pores as many discrete clusters. The brine clusters were not well connected between the inlet and outlet, especially as filling of the restrictions (throats) between pores is not favoured in oil-wet regions. The brine flowed through the microporosity, which is the reason why the brine relative permeability remained very low. As the fractional flow increased from $f_w = 0.05$ to $f_w = 0.5$, the brine saturation increased slightly by 5% and the connectivity of brine clusters increased gradually but the brine at the outlet remained poorly connected. As shown in Fig. 12 and Table 3, the water relative

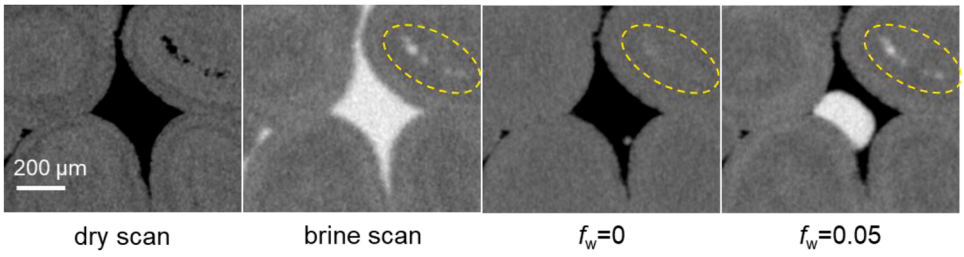

Fig. 13. Images of one pore space at the same position for different fractional flows. The yellow ellipses indicate brine in microporosity.

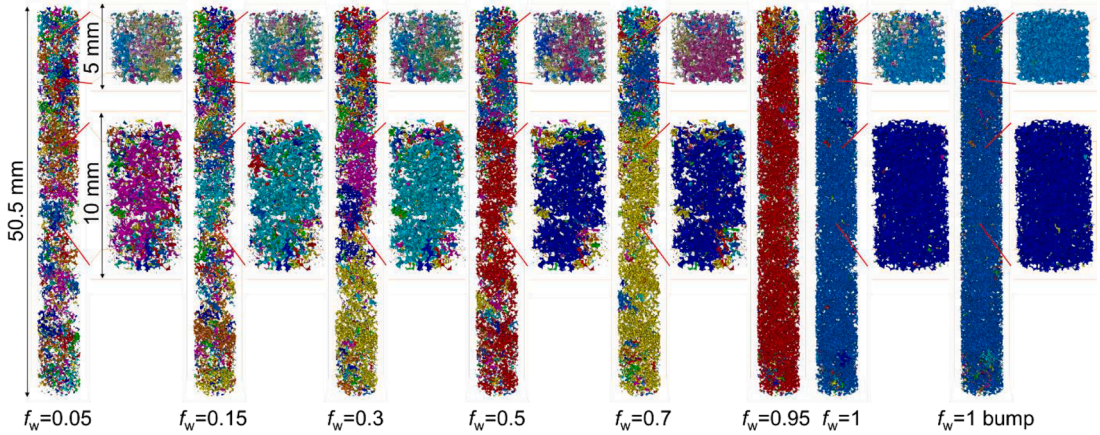

Fig. 14. Three-dimensional volume rendering of the brine phase in macropores at different fractional flows, showing the development of brine phase connectivity. Different colours represent discrete ganglia of brine. The stitched three-dimensional volume rendering of the full sample with voxel size of 8.91 μm is shown on the left and smaller volumes in the middle and near the flow outlet of the sample with voxel size of 3.58 μm are shown on the right for each fractional flow.

Table 4
The brine connectivity in macropores in a smaller volume in the middle of the sample with voxel size of 3.58 μm. The connectivity is defined as the ratio between the volume of the connected brine from the bottom to the top and the total volume of brine.

f_w	Brine connectivity in macropores
0.05	0.447
0.15	0.612
0.3	0.793
0.5	0.828
0.7	0.842
1	0.993

permeability was almost constant, as the brine flow was maintained by the microporosity of the Ketton limestone (with pore sizes of less than 0.1 μm, Fig. 1). From $f_w = 0.5$ to $f_w = 0.7$, there is a slight increase in brine saturation and connectivity especially at the outlet, corresponding to a small rise in the water relative permeability. At $f_w = 0.95$, a critical point, the water relative permeability started to increase sharply as the brine phase formed a connected path. At the last point, $f_w = 1$, the pump flow rate was increased 100 times (bump flood) and finally the brine invaded small throats and broke through in the macropores. Thus, the brine occupied most of the pore space and consequently was well connected with a high relative permeability of 0.66.

Fig. 14 also illustrates the importance of accounting for saturation heterogeneity. We calculate our relative permeabilities based on a slice-averaged saturation. Had we instead used the average saturation of the whole sample, where the water was poorly connected near the outlet, we would have significantly underestimated the relative permeability, as demonstrated in Table 3.

3.6.3. *Relative permeability comparison with different carbonates*

We compared the relative permeability characteristics of Ketton carbonate with previously published results on an oil-wet Estaillades carbonate (Lin et al., 2021) and a mixed-wet reservoir carbonate (Alhammadi et al., 2020) (Fig. 15): see Fig. 11b for a comparison of the capillary pressures of these samples. By comparing the pore size distributions of these three carbonates, we can see Ketton and Estaillades have more microporosity than the reservoir carbonate. This explains why the initial water saturation in these two samples is higher.

Ketton carbonate is a remarkable example of rock with relatively uniformly distributed microporosity; a separation of scales exists between large inter-granular pores (>10 μm) and microporosity (<0.1 μm) inside the grains, see Fig. 1 (Bijeljic et al., 2018). When the saturation is low, below 0.6, brine in the macropores was poorly connected with few large clusters (see Fig. 14) and the relative permeability was exceptionally low (<0.01) limited by flow through microporosity. Once the brine clusters connected through the macropores, the relative permeability increased significantly with a high end-point water relative permeability of 0.66. As discussed above, the displacement is percolation-like and the relative permeability has mixed-wet characteristics. Similar behaviour – namely a low and almost constant water relative permeability for low and intermediate saturations followed by a rapid rise when the water connects in microporosity – is observed in the reservoir carbonate (Alhammadi et al., 2020); however, in this case the amount of microporosity was lower, with a lower initial water saturation, and so the relative permeabilities are shifted to the left and stretched in comparison to Ketton.

In contrast, Estaillades carbonate has a more complex sub-micron pore space with a large range of pore sizes. Its sub-resolution microporosity can allow more flow leading to a more rapid rise in relative permeability with water saturation. Estaillades carbonate has a significant fraction of macropores that are connected only through sub-resolution microporosity (Fig. 3) and it has a much higher initial water saturation and water relative permeability at the beginning of waterflooding. The ability of the microporosity to allow significant flow, combined with the more oil-wet nature of the macropores (see the capillary pressures in Fig. 11b) lead to an invasion-percolation like displacement and more oil-wet relative permeability characteristics (Lin et al., 2021).

In summary, wettability and pore size distribution, and particularly the role of microporosity, control the relative permeability characteristics of these carbonates. The use of high-resolution imaging and analysis allows us to understand and interpret the different behaviour in terms of pore-scale displacement processes.

4. Conclusions

We used a suite of experimental and image analysis tools to measure relative permeability and capillary pressure simultaneously on an altered-wettability carbonate with distinct bimodal porosity.

We used a greyscale-based differential imaging method which provides accurate porosity and saturation measurements without image segmentation. We demonstrated the measured porosity and saturation

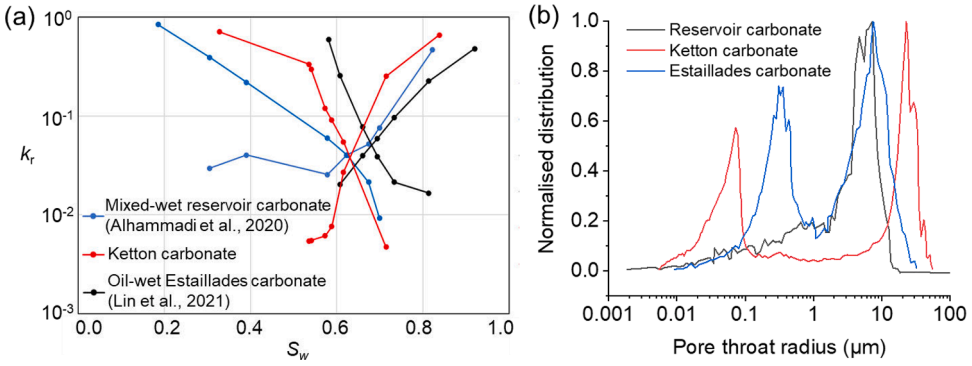

Fig. 15. (a) Comparison between the mean of the corrected relative permeability from this work on Ketton and previously published measurements on mixed-wet reservoir carbonate (Alhammadi et al., 2020) and oil-wet Estlaillades carbonate (Lin et al., 2021). (b) Pore size distributions for these three carbonate rocks.

profile from the coarser resolution images is consistent slice by slice with the high-resolution ones, which implies the greyscale-based differential imaging method is accurate even at voxel sizes of approximately 9 μm. The measured relative permeability values were corrected by considering the variation in slice-averaged saturation along the flow direction. We found both brine and oil relative permeability values were underestimated by simply using average saturation values in the k_r-S_w relationship, which assumes a uniform saturation profile in the sample for each fractional flow.

The resolvable macropores displayed an overall oil-wet behaviour, measured from contact angle, fluid occupancy, curvature and capillary pressure on micro-CT images. The oil-brine interfaces had a small negative mean curvature, implying a low negative capillary pressure. We observed many saddle-shape oil-brine interfaces with nearly equal but opposite principal curvatures in orthogonal direction. This implies that oil and brine phases preserve good connectivity during the experiments.

Ketton limestone wettability and bimodal pore size distribution explain the relative permeability behaviour, which is different from other carbonate rocks. Pore-space images show that brine initially flowed through microporosity and was then forced to fill the centre of large oil-wet pores. The brine clusters were not well connected initially through the macropores and instead the flow was maintained through microporosity. The oil relative permeability dropped quickly as oil was drained to low saturation and flowed through connected oil layers. The brine flowed through microporosity and its relative permeability remained very low until brine invaded small throats and formed a connected flow path through the macropores at which point the brine relative permeability increased significantly.

We propose that this experimental and analysis workflow could be used to characterize and interpret displacement behaviour in a range of porous materials.

CRediT authorship contribution statement

Guanglei Zhang: Conceptualization, Investigation, Formal analysis, Writing – original draft. **Sajjad Foroughi:** Investigation, Formal analysis. **Ali Q. Raeini:** Investigation, Formal analysis. **Martin J. Blunt:** Conceptualization, Supervision, Writing – review & editing. **Branko Bijeljic:** Conceptualization, Supervision, Writing – review & editing.

Declaration of Competing Interest

The authors declare that they have no known competing financial interests or personal relationships that could have appeared to influence the work reported in this paper.

Data availability

: Data will be made available on request.

Acknowledgments

We acknowledge TotalEnergies for providing the financial support to this experiment and for fruitful technical discussions with their digital rock physics team. We also thank Qingyang Lin (Zhejiang University) for sharing image processing scripts. Branko Bijeljic is also very grateful to TotalEnergies for funding his Senior Fellowship.

Appendix A. Contrast scan between rock and fluids

Contrast scans between rock and fluids were taken before the experiment. Ketton limestone particles were put into four small glass bottles. 7 wt%, 15 wt%, 20 wt% and 25 wt% KI brine was prepared and poured into the bottles. Then decane was put inside each bottle and well mixed with brine and rock particles. Quick scans (801 projections) were taken for the bottles with rock and fluids. By comparing the contrast of the rock, oil, and brine (Figs. A1 and A2), 25 wt% KI brine was chosen as the optimum brine salinity for image contrast.

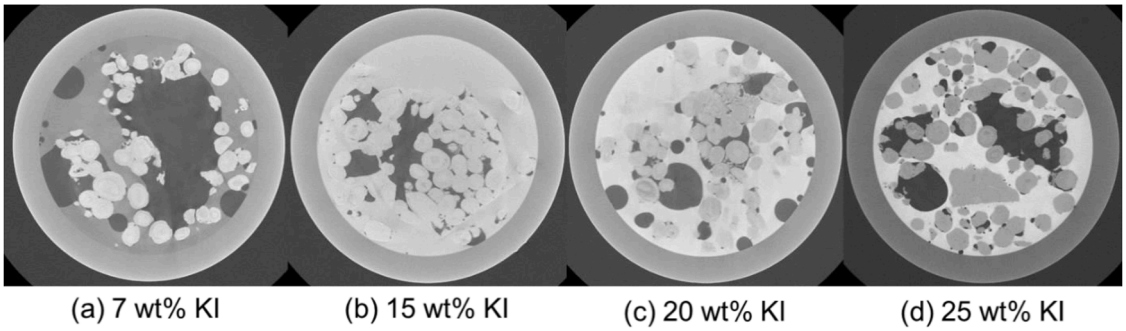

Fig. A1. Contrast scans between rock and fluids. (a) Using 7 wt% KI in water, it is possible to distinguish water, oil and rock phases, and water is the intermediate phase between oil and rock. (b) Using 15 wt% KI in water, water is not distinguishable from rock. (c) Using 20 wt% KI, water can be distinguished from rock, but the contrast is insufficient for accurate quantitative analysis. (d) Using 25 wt% KI, it is possible to distinguish three phases and the contrast is better. The last option was chosen for the full experiment.

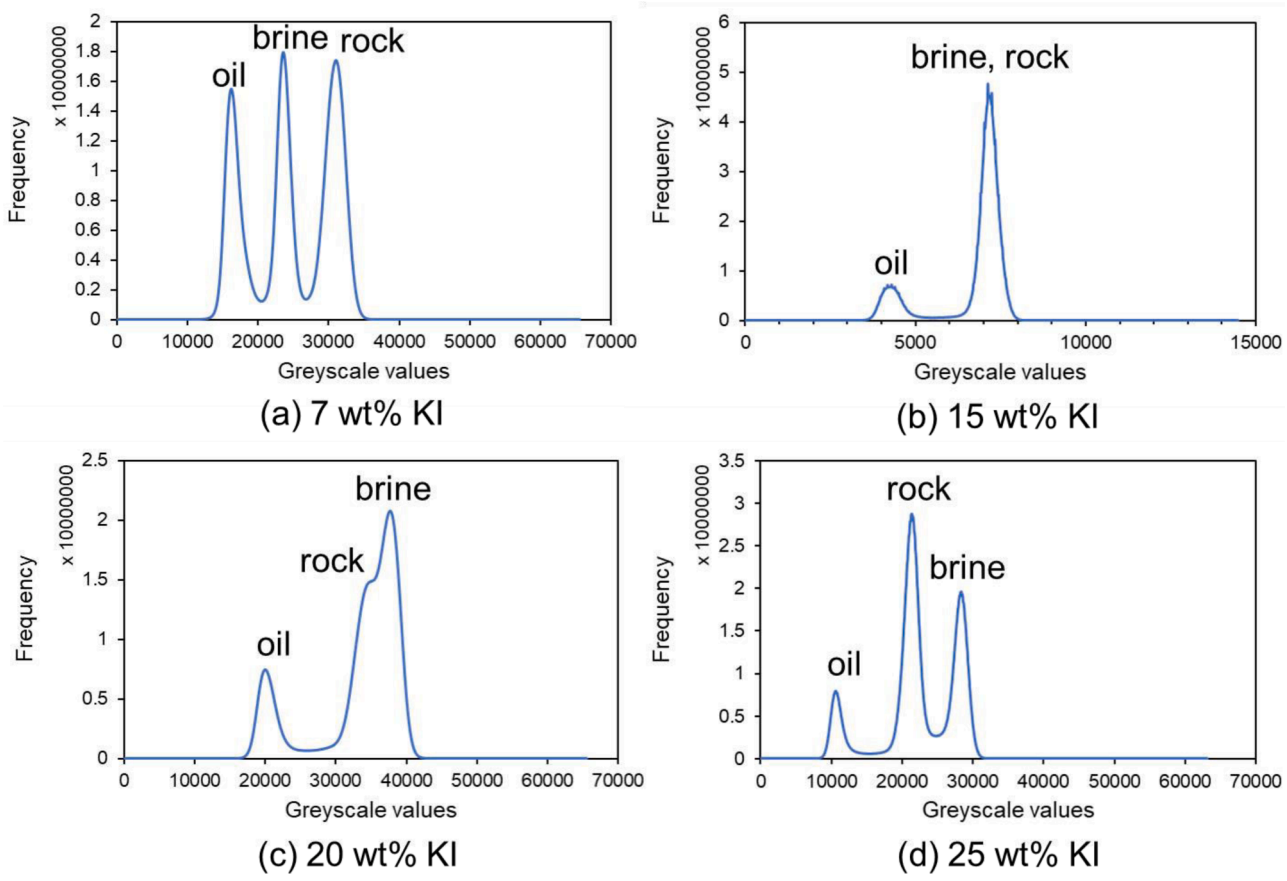

Fig. A2. Histograms of the grey scale values of the contrast scans.

Appendix B. Tubing pressure validation for single-phase flow

For a circular tube, Poiseuille's equation for flow is

$$Q = \frac{\pi r^4}{8\mu}\frac{\Delta p}{L} \tag{B1}$$

where Q is the flow rate; r is the tube radius; Δp is the pressure loss over length L; μ is the fluid viscosity.

From Darcy's law,

$$Q = \frac{kA}{\mu}\frac{\Delta p}{L} \tag{B2}$$

where A is the tube area (πr^2). By analogy with Darcy's law Eq. (B2), the absolute permeability of a circular tube can be derived from Eq. (B1)

$$k = \frac{r^2}{8} \tag{B3}$$

The absolute permeability can be calculated analytically based on Eq. (B3). We know $r = 0.38$ mm, and then we can calculate $k = 1.81 \times 10^{-8}\, m^2$.

We have also experimentally measured absolute permeability by single oil phase flow. The tube and fluid properties are as follows

μ=0.838×10^{-3}*Pa.s*
Q=0.4mL/min=6.67×10^{-9}m^3/s
A=πr^2=3.14×0.38^{2}mm^2=4.53×10m^2
L=2.0m
Δp=1340 Pa

Based on Darcy' law, the experimentally measured absolute permeability is

$$k = \frac{Q\mu L}{A\Delta p} = 1.84 \times 10^{-8} m^2$$

The experimentally measured absolute permeability agrees well with the theoretical one derived from the Poiseuille's equation. This demonstrated our tubing pressure measurement is accurate, at least for single-phase flow.

Appendix C. Tubing pressure uncertainty for multiphase flow

The measured total pressures, tube pressures and associated uncertainties at each fractional flow are shown in Table C1. The core pressure, which was the difference between total pressure and tube pressure at each fractional flow, is used for the relative permeability calculation. As the tube pressure was measured after removing the sample from core holder, these values may not be the same as the tube pressures when there was rock present. Therefore, there is uncertainty with the tube pressure measurement. To properly assess the uncertainties, the ratio of the tube pressure and the total pressure was calculated at each fractional flow and the ratio ranges from 0.13 to 0.36. We assume the real tube pressures ranges from 0.13 to 0.36 of total pressures for all fractional flows.

Table C1
The measured total pressures and tube pressures at each fractional flow.

f_w	Total pressure, kPa	Tube pressure, kPa	Core pressure, kPa	Ratio of the tube pressure and the total pressure
0	0.75 ± 0.04	0.13	0.61	0.18
0.05	5.94 ±1.22	2.22	3.72	0.37
0.15	21.32 ± 0.47	7.57	13.75	0.36
0.3	34.84 ± 0.50	12.68	22.16	0.36
0.5	37.27 ± 0.68	8.01	29.26	0.21
0.7	30.17 ± 0.90	7.81	22.36	0.26
0.95	8.08 ± 2.11	2.84	5.24	0.35
1	0.83 ± 0.07	0.11	0.72	0.13

Appendix D. Greyscale-based differential imaging to compute porosity and saturation

The porosity can be estimated based on the CT numbers (greyscale values) of the phases in the dry image:

$$\bar{CT} = CT_{rock}(1-\phi) + CT_{air}\phi \tag{D1}$$

$$\phi = \frac{\bar{CT} - CT_{rock}}{CT_{air} - CT_{rock}} \tag{D2}$$

where ϕ is the porosity, $\bar{CT}$represents the average CT number of the whole image, CT_{rock} and CT_{air} are the representative CT number of solid and air phases, respectively.

Similarly, fluid saturations can be estimated based on the on the CT numbers of the phases in partially-saturated images – containing oil and brine and solid:

$$\bar{CT} = CT_{rock}(1-\phi) + CT_o\phi S_o + CT_w\phi(1-S_o) \tag{D3}$$

$$S_o = \frac{\bar{CT} - CT_{rock}(1-\phi) - CT_w\phi}{(CT_o - CT_w)\phi} \tag{D4}$$

where $\bar{CT}$ represents the average CT number of the whole image, CT_{rock}, CT_{o} and CT_{w} are the representative CT number of solid, oil and water phases, respectively.

During differential imaging (Figs. D1 and D2) – subtracting the brine saturated image from the dry/partially-saturated images – the solid and brine phases cancel out reducing the uncertainty. Therefore, Eqs. (D2) and (D4) can be written for the differential images as:

$$\phi = \frac{\bar{CT}}{CT_{air}} \tag{D5}$$

$$S_o = \frac{\bar{CT}}{CT_o\phi} \tag{D6}$$

One key procedure for differential imaging is greyscale normalization to make sure the greyscale values are consistent for the same phases for the images at every fractional flow. To achieve this, we normalized all the greyscale images to the brine scan slice by slice by using non-microporous rock and the Viton sleeve as masks. The uncertainty in porosity and saturation were obtained based on variations of greyscale values for different fluids (CT_{air} and CT_{o} in Eqs. D5 and D6). Increasing the contrast between brine and oil can lead to lower uncertainty. However, there is a trade-off as doping the brine to be excessively opaque to X-rays leads to lower image quality and increased image blur at the boundary between phases. 25% KI was selected after conducting contrast scans between rock and fluids; see the details in Appendix A.

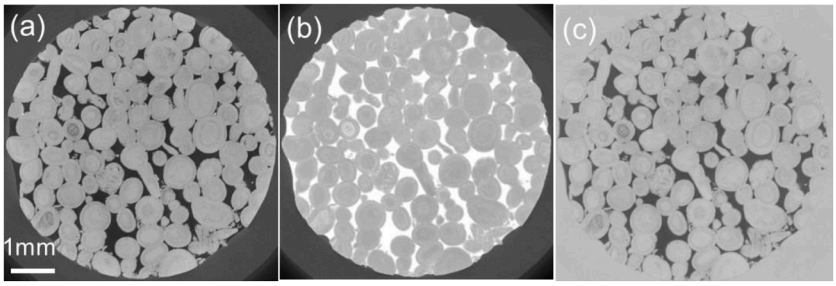

Fig. D1. Two-dimensional slices of three-dimensional images at the same location in the Ketton sample. (a) The dry scan. Air in the pore space is X-ray transparent shown black. (b) The brine-saturated image. Brine has a higher X-ray attenuation than grains and appears bright (white) in the image. (c) The differential image between dry scan (a) and brine scan (b), where a constant number of 30000 was added to avoid negative values. The solid phase cancels out during differential imaging and is light grey in the image. Macropores are in black and the unresolved microporosity appears dark grey.

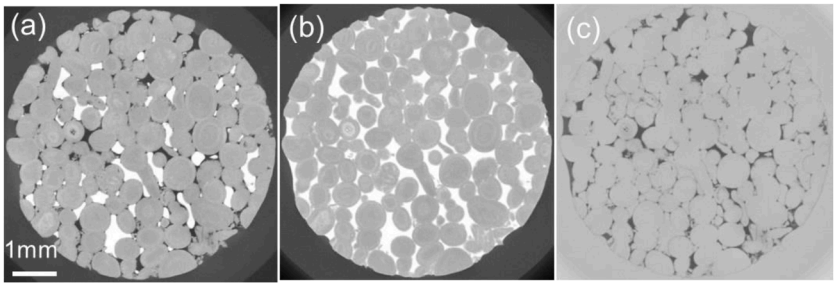

Fig. D2. Two-dimensional slices of three-dimensional images at the same location in the Ketton sample. (a) The partially-saturated image – containing oil (black) and brine (white) and solid (grey). (b) The brine-saturated image. (c) The differential image between the partially saturated image (a) and the brine scan (b), where a constant number of 30000 was added to avoid negative values. The solid and brine phases cancel out during differential imaging, shown light grey in the image. The oil phase is black.

Appendix E. Greyscale image segmentation

Greyscale images with a voxel size of 3.58 μm for each fractional flow are illustrated in Fig. E1. Black is oil, grey is rock grain (solid), and white is brine. The macropore space and rock phases were segmented firstly from the differential image of dry and brine scans (Fig. D1). The high salinity brine was even brighter than the solid and the differential image helps distinguish solid and macropores. Macropores can be easily segmented from the rock using the interactive thresholding method without segmenting microporous grains where a complex segmentation method is needed (*Lin et al.*, 2016). The next step was to segment oil in the macropores. Similarly, oil in the macropores was segmented from the differential image between the multiphase scans and the high salinity brine scan (Fig. D2) using the interactive thresholding method based on the greyscale values. The segmented oil phase was masked by the solid and the remaining phase was brine. The segmented images are shown in Fig. E2, where the grey is solid with microporosity and the fluids in the macropores were segmented into brine (blue) and oil (red).

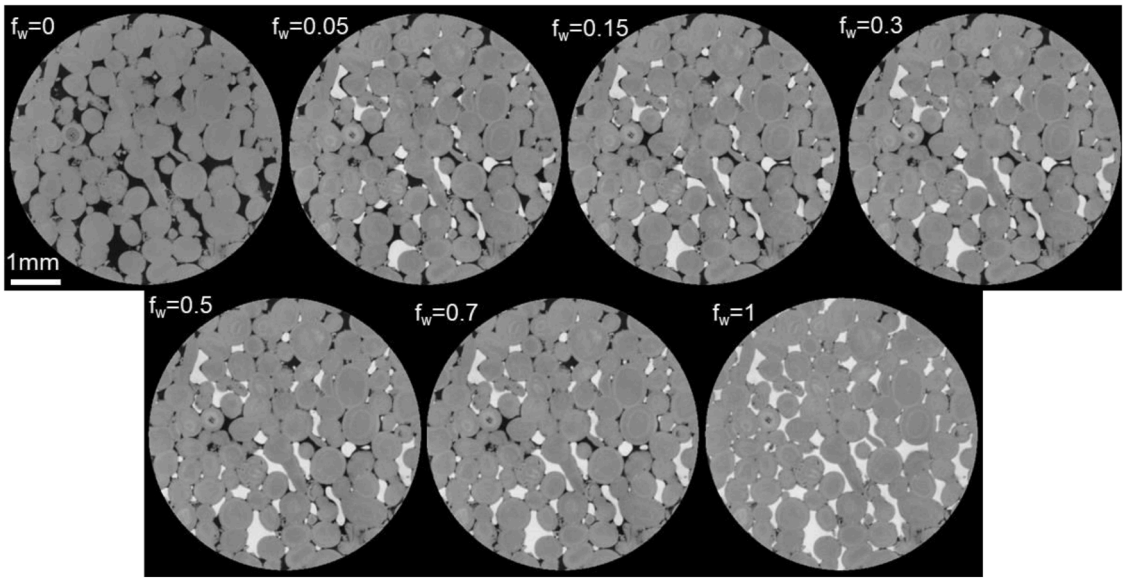

Fig. E1. Two-dimensional cross-sectional views of three-dimensional X-ray images of the same slice at each fractional flow for Ketton limestone. The oil, rock and brine are shown in black, grey and white respectively. Note the image at fractional flow $f_w = 0.95$ was not included here as we could not achieve steady state when the image was taken.

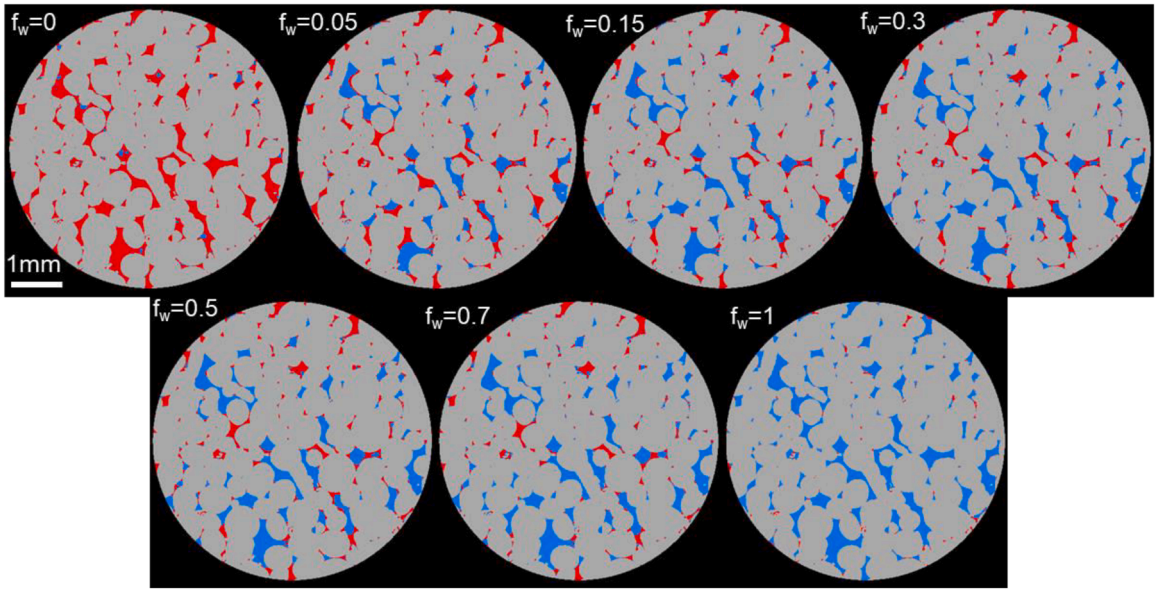

Fig. E2. Two-dimensional cross-sectional views of the segmented image, corresponding to Fig. 6, showing brine (blue), oil (red) and rock (grey) of the same slice at each fractional flow.

Appendix F. Relative permeability correction method for inhomogeneous saturation profiles

In this two-phase flow experiment, the fluid flow is upward. For any fractional flow the multiphase Darcy's law for one-dimensional vertical flow is

$$q_o = -\frac{Kk_{ro}}{\mu_o}\left(\frac{\partial P_o}{\partial x} + \rho_o g\right) \tag{F1}$$

$$q_w = -\frac{Kk_{rw}}{\mu_w}\left(\frac{\partial P_w}{\partial x} + \rho_w g\right) \tag{F2}$$

$$P_c = P_o - P_w \tag{F3}$$

where the subscripts o and w stand for oil and water respectively, q is the Darcy velocity, K is the absolute permeability, k_r is the relative permeability, μ is the viscosity, P is the fluid pressure, x is the distance along the flow direction, ρ is the fluid density, g is the gravitational acceleration, and P_c is the capillary pressure.

By integrating Eqs. (F1) and (F2) between sample length from 0 and L, the pressure drop, ΔP, across the sample length, which was measured in the oil phase, is given by:

$$\Delta P = \Delta P_o = \frac{\mu_o q_o}{K}\int_0^L \frac{1}{k_{ro}(S_w)}dx + \rho_o g L \tag{F4}$$

$$\Delta P = \Delta P_o = \frac{\mu_w q_w}{K}\int_0^L \frac{1}{k_{rw}(S_w)}dx + \rho_w g L + P_c(x=0) - P_c(x=L) \tag{F5}$$

where relative permeability is assumed to be a unique function of saturation: $k_r(S_w)$ and we assume that the absolute permeability is constant.

We estimated the initial water saturation (S_{wi}) and the residual oi saturation (S_{or}) from the lowest slice-averaged saturations of water and oil observed in the experiments. We divided the saturation evenly across the saturation range from S_{wi} to 1-S_{or} into eight increments. Then we described the oil and water relative permeability using eight unknown values at the eight discrete points: $k_{ro,i}$ and $k_{rw,i}$, with i from 1 to 8. For any saturation value, we were able to define the relative permeability by linearly interpolating between the eight discrete values. As we have obtained the slice-by-slice saturation profile (Fig. 5), a unique relative permeability as a function of saturation can be defined locally in slice-averages of the image, and the integral in Eqs. (F4) and (F5) can be replaced by linear sums as

$$\Delta P_i = \frac{\mu_o q_{o,i}}{K}\Delta x\sum_{j=1}^{n}\frac{1}{k_{ro}\left(S_w^{i,j}\right)} + \rho_o g L \tag{F6}$$

$$\Delta P_i = \frac{\mu_w q_{w,i}}{K}\Delta x\sum_{j=1}^{n}\frac{1}{k_{rw}\left(S_w^{i,j}\right)} + \rho_w g L + P_{c,i}(x=0) - P_{c,i}(x=L) \tag{F7}$$

where Δx is every increment of sample length in the image, which is the voxel size, j is the slice number of images along the measured saturation

profile, n is the total number of the slices. Here i labels the fractional flow: we have eight different measured pressure differences.

In Eqs. (F6) and (F7), we account for pressure differences between the phases due to differences in capillary pressure and buoyancy. We assume the capillary pressure at the inlet is the same as the values obtained from the high-resolution image in the middle of the sample which we have measured – see Fig. 11b, whereas the capillary pressure at the outlet is zero due to the capillary end effect. We then find the relative permeability which, when the pressure gradient is integrated along the measured saturation profile, gives the measured overall pressure drop to within the uncertainty of the measurements, see Appendix C. This is an optimization process which leads to a range of possible relative permeability values, as presented in the main text.

References

Akbarabadi, M., Piri, M., 2013. Relative permeability hysteresis and capillary trapping characteristics of supercritical CO_2/brine systems: an experimental study at reservoir conditions. Adv. Water Res. 52, 190–206.

Alhammadi, A.M., AlRatrout, A., Singh, K., Bijeljic, B., Blunt, M.J., 2017. In situ characterization of mixed-wettability in a reservoir rock at subsurface conditions. Sci. Rep. 7 (1), 1–9.

Alhammadi, A.M., Gao, Y., Akai, T., Blunt, M.J., Bijeljic, B., 2020. Pore-scale X-ray imaging with measurement of relative permeability, capillary pressure and oil recovery in a mixed-wet micro-porous carbonate reservoir rock. Fuel 268, 117018.

AlRatrout, A., Blunt, M.J., Bijeljic, B., 2018. Wettability in complex porous materials, the mixed-wet state, and its relationship to surface roughness. Proc. Natl. Acad. Sci. 115 (36), 8901–8906.

AlRatrout, A., Raeini, A.Q., Bijeljic, B., Blunt, M.J., 2017. Automatic measurement of contact angle in pore-space images. Adv. Water Res. 109, 158–169.

Andreas, J., Hauser, E., Tucker, W., 1938. Boundary tension by pendant drops1. J. Phys. Chem. 42 (8), 1001–1019.

Andrew, M., Bijeljic, B., Blunt, M.J., 2014a. Pore-scale contact angle measurements at reservoir conditions using X-ray microtomography. Adv. Water Res. 68, 24–31.

Andrew, M., Bijeljic, B., Blunt, M.J., 2014b. Pore-by-pore capillary pressure measurements using X-ray microtomography at reservoir conditions: curvature, snap-off, and remobilization of residual CO 2. Water Resour. Res. 50 (11), 8760–8774.

Andrew, M., Menke, H., Blunt, M.J., Bijeljic, B., 2015. The imaging of dynamic multiphase fluid flow using synchrotron-based X-ray microtomography at reservoir conditions. Transp. Porous Media 110 (1), 1–24.

Armstrong, R.T., Porter, M.L., Wildenschild, D., 2012. Linking pore-scale interfacial curvature to column-scale capillary pressure. Adv. Water Res. 46, 55–62.

Arns, C.H., Bauget, F., Limaye, A., Sakellariou, A., Senden, T.J., Sheppard, A.P., Sok, R. M., Pinczewski, W.V., Bakke, S., Berge, L.I., Øren, P.E., Knackstedt, M.A., 2005. Pore-scale characterization of carbonates using X-ray microtomography. SPE J. 10 (04), 475–484.

Bear, J., Cheng, A.H.-D., 2010. Modeling Groundwater Flow and Contaminant Transport. Springer.

Benson, S.M., Cole, D.R., 2008. CO2 sequestration in deep sedimentary formations. Elements 4 (5), 325–331.

Berg, S., Ott, H., Klapp, S.A., Schwing, A., Neiteler, R., Brussee, N., Makurat, A., Leu, L., Enzmann, F., Schwarz, J.-O., 2013. Real-time 3D imaging of Haines jumps in porous media flow. Proc. Natl. Acad. Sci. 110 (10), 3755–3759.

Bijeljic, B., A. Q. Raeini, Q. Lin, and M. J. Blunt (2018), Multimodal functions as flow signatures in complex porous media, *arXiv preprint arXiv:1807.07611*.

Blunt, M.J., 2017. Multiphase Flow in Permeable Media: A Pore-Scale Perspective. Cambridge university press.

Blunt, M.J., Bijeljic, B., Dong, H., Gharbi, O., Iglauer, S., Mostaghimi, P., Paluszny, A., Pentland, C., 2013. Pore-scale imaging and modelling. Adv. Water Res. 51, 197–216.

Blunt, M.J., Lin, Q., Akai, T., Bijeljic, B., 2019. A thermodynamically consistent characterization of wettability in porous media using high-resolution imaging. J. Colloid Interface Sci. 552, 59–65.

Boot-Handford, M.E., Abanades, J.C., Anthony, E.J., Blunt, M.J., Brandani, S., Dowell, N. Mac, Fernández, J.R., Ferrari, M.-C., Gross, R., Hallett, J.P., 2014. Carbon capture and storage update. Energy Environ. Sci. 7 (1), 130–189.

Bultreys, T., Van Hoorebeke, L., Cnudde, V, 2015. Multi-scale, micro-computed tomography-based pore network models to simulate drainage in heterogeneous rocks. Adv. Water Res. 78, 36–49.

Dong, H., Blunt, M.J., 2009. Pore-network extraction from micro-computerized-tomography images. Phys. Rev. E 80 (3), 036307.

Gao, Y., Lin, Q., Bijeljic, B., Blunt, M.J., 2017. X-ray microtomography of intermittency in multiphase flow at steady state using a differential imaging method. Water Resour. Res. 53 (12), 10274–10292.

Gao, Y., Raeini, A.Q., Blunt, M.J., Bijeljic, B., 2019. Pore occupancy, relative permeability and flow intermittency measurements using X-ray micro-tomography in a complex carbonate. Adv. Water Res. 129, 56–69.

Gao, Y., Raeini, A.Q., Blunt, M.J., Bijeljic, B., 2021. Dynamic fluid configurations in steady-state two-phase flow in Bentheimer sandstone. Phys. Rev. E 103 (1), 013110.

Gao, Y., Raeini, A.Q., Selem, A.M., Bondino, I., Blunt, M.J., Bijeljic, B., 2020. Pore-scale imaging with measurement of relative permeability and capillary pressure on the same reservoir sandstone sample under water-wet and mixed-wet conditions. Adv. Water Res. 146, 103786.

Garing, C., de Chalendar, J.A., Voltolini, M., Ajo-Franklin, J.B., Benson, S.M., 2017. Pore-scale capillary pressure analysis using multi-scale X-ray micromotography. Adv. Water Res. 104, 223–241.

Gerritsen, M.G., Durlofsky, L.J., 2005. Modeling fluid flow in oil reservoirs. Annu. Rev. Fluid Mech. 37, 211.

Jackson, S.J., Agada, S., Reynolds, C.A., Krevor, S., 2018. Characterizing drainage multiphase flow in heterogeneous sandstones. Water Resour. Res. 54 (4), 3139–3161.

Khanamiri, H.H., Berg, C.F., Slotte, P.A., Schlüter, S., Torsæter, O., 2018. Description of free energy for immiscible two-fluid flow in porous media by integral geometry and thermodynamics. Water Resour. Res. 54 (11), 9045–9059.

Klise, K.A., Moriarty, D., Yoon, H., Karpyn, Z., 2016. Automated contact angle estimation for three-dimensional X-ray microtomography data. Adv. Water Res. 95, 152–160.

Krevor, S.C., Pini, R., Zuo, L., Benson, S.M., 2012. Relative permeability and trapping of CO_2 and water in sandstone rocks at reservoir conditions. Water Resour. Res. 48 (2).

Lin, Q., Al-Khulaifi, Y., Blunt, M.J., Bijeljic, B., 2016. Quantification of sub-resolution porosity in carbonate rocks by applying high-salinity contrast brine using X-ray microtomography differential imaging. Adv. Water Res. 96, 306–322.

Lin, Q., Bijeljic, B., Berg, S., Pini, R., Blunt, M.J., Krevor, S., 2019. Minimal surfaces in porous media: pore-scale imaging of multiphase flow in an altered-wettability Bentheimer sandstone. Phys. Rev. E 99 (6), 063105.

Lin, Q., Bijeljic, B., Foroughi, S., Berg, S., Blunt, M.J., 2021. Pore-scale imaging of displacement patterns in an altered-wettability carbonate. Chem. Eng. Sci. 235, 116464.

Lin, Q., Bijeljic, B., Pini, R., Blunt, M.J., Krevor, S., 2018. Imaging and measurement of pore-scale interfacial curvature to determine capillary pressure simultaneously with relative permeability. Water Resour. Res. 54 (9), 7046–7060.

Niu, X.-D., Munekata, T., Hyodo, S.-A., Suga, K., 2007. An investigation of water-gas transport processes in the gas-diffusion-layer of a PEM fuel cell by a multiphase multiple-relaxation-time lattice Boltzmann model. J. Power Sources 172 (2), 542–552.

Pak, T., Butler, I.B., Geiger, S., Van Dijke, M.I., Sorbie, K.S., 2015. Droplet fragmentation: 3D imaging of a previously unidentified pore-scale process during multiphase flow in porous media. Proc. Natl. Acad. Sci. 112 (7), 1947–1952.

Pak, T., Butler, I.B., Geiger, S., Van Dijke, M.I., Jiang, Z., Surmas, R., 2016. Multiscale pore-network representation of heterogeneous carbonate rocks. Water Resour. Res. 52 (7), 5433–5441.

Parker, J., 1989. Multiphase flow and transport in porous media. Rev. Geophys. 27 (3), 311–328.

Pini, R., Madonna, C, 2016. Moving across scales: a quantitative assessment of X-ray CT to measure the porosity of rocks. J. Porous Mater. 23 (2), 325–338.

Raeini, A.Q., Bijeljic, B., Blunt, M.J., 2017. Generalized network modeling: network extraction as a coarse-scale discretization of the void space of porous media. Phys. Rev. E 96 (1), 013312.

Raeini, A.Q., Giudici, L.M., Blunt, M.J., Bijeljic, B., 2022. Generalized network modelling of two-phase flow in a water-wet and mixed-wet reservoir sandstone: uncertainty and validation with experimental data. Adv. Water Res. 164, 104194.

Rücker, M., Bartels, W.B., Singh, K., Brussee, N., Coorn, A., van der Linde, H.A., Bonnin, A., Ott, H., Hassanizadeh, S.M., Blunt, M.J., 2019. The effect of mixed wettability on pore-scale flow regimes based on a flooding experiment in Ketton limestone. Geophys. Res. Lett. 46 (6), 3225–3234.

Scanziani, A., Lin, Q., Alhosani, A., Blunt, M.J., Bijeljic, B., 2020. Dynamics of fluid displacement in mixed-wet porous media. Proc. R. Soc. A 476 (2240), 20200040.

Scanziani, A., Singh, K., Blunt, M.J., Guadagnini, A., 2017. Automatic method for estimation of in situ effective contact angle from X-ray micro tomography images of two-phase flow in porous media. J. Colloid Interface Sci. 496, 51–59.

Selem, A.M., Agenet, N., Gao, Y., Raeini, A.Q., Blunt, M.J., Bijeljic, B., 2021. Pore-scale imaging and analysis of low salinity waterflooding in a heterogeneous carbonate rock at reservoir conditions. Sci. Rep. 11 (1), 1–14.

Spurin, C., Bultreys, T., Rücker, M., Garfi, G., Schlepütz, C.M., Novak, V., Berg, S., Blunt, M.J., Krevor, S., 2021. The development of intermittent multiphase fluid flow pathways through a porous rock. Adv. Water Res. 150, 103868.

Stauffer, C.E., 1965. The measurement of surface tension by the pendant drop technique. J. Phys. Chem. 69 (6), 1933–1938.

Sun, C., McClure, J.E., Mostaghimi, P., Herring, A.L., Berg, S., Armstrong, R.T., 2020. Probing effective wetting in subsurface systems. Geophys. Res. Lett. 47 (5) no-no.

Vega, B., Dutta, A., Kovscek, A.R., 2014. CT imaging of low-permeability, dual-porosity systems using high X-ray contrast gas. Transp. Porous Media 101 (1), 81–97.

Wildenschild, D., Sheppard, A.P., 2013. X-ray imaging and analysis techniques for quantifying pore-scale structure and processes in subsurface porous medium systems. Adv. Water Res. 51, 217–246.
Withjack, E.M., 1988. Computed tomography for rock-property determination and fluid-flow visualization. SPE Form. Eval. 3 (04), 696–704.
Zivar, D., Kumar, S., Foroozesh, J., 2021. Underground hydrogen storage: a comprehensive review. Int. J. Hydrog. Energy 46 (45), 23436–23462.
Zou, S., Armstrong, R.T., Arns, J.Y., Arns, C.H., Hussain, F., 2018a. Experimental and theoretical evidence for increased ganglion dynamics during fractional flow in mixed-wet porous media. Water Resour. Res. 54 (5), 3277–3289.
Zou, S., Hussain, F., Arns, J.-y., Guo, Z., Arns, C.H., 2018b. Computation of relative permeability from in-situ imaged fluid distributions at the pore scale. SPE J. 23 (03), 737–749.